Circulating proteome of hospitalized patients uncovers six endophenotypes of COVID-19 and points to FGFR and SHC4-signaling in acute respiratory distress syndrome

William Ma[1,*], Antoine Soulé[1,*], Katelyn Yixiu Liu[2], Catherine Allard[3], Karine Tremblay[4, †], Simon Rousseau[2, †], and Amin Emad[1, 5, †]

[*] These authors contributed equally.

[1] Department of Electrical and Computer Engineering, McGill University, Montréal, QC, Canada

[2] The Meakins-Christie Laboratories at the Research Institute of the McGill University Heath Centre Research Institute, & Department of Medicine, Faculty of Medicine, McGill University, Montréal, QC, Canada

[3] Statistical department, Centre de recherche du Centre hospitalier universitaire de Sherbrooke (CRCHUS), Sherbrooke, Canada.

[4] Pharmacology-physiology Department, Faculty of Medicine and Health Sciences, Université de Sherbrooke, Saguenay, QC, Canada; Centre intégré universitaire de santé et de services sociaux du Saguenay-Lac-Saint-Jean, Saguenay, QC, Canada; CRCHUS, Sherbrooke, Canada.

[5] Mila, Quebec AI Institute, Montréal, QC, Canada

† Corresponding Authors:
Amin Emad,
755 McConnell Engineering Building, 3480 University Street, Montreal H3A 0E9, Canada
Email: amin.emad@mcgill.ca

Simon Rousseau,
RI-MUHC, E M3.2244, 1001 Décarie, Montréal H4A 3J1, Canada,
Email: simon.rousseau@mcgill.ca

Karine Tremblay,
Pavillon des Augustines, local AUG-5-01A, 225 St-Vallier street, Chicoutimi G7H 7P2, Canada
Email: karine.tremblay@usherbrooke.ca

Abstract

Defining the molecular mechanisms of novel diseases such as COVID-19 is crucial to identify treatable traits to improve patient care. To circumvent *a priori* bias and the lack of in-depth knowledge of this new disease, we opted for an unsupervised stratification approach, followed by detailed multi-modal characterization using proteome, metabolomic, genomic, and clinical features. Using the detailed circulating proteome, as measured by 4985 aptamers (SOMAmers), robust consensus clustering identified six endophenotypes (EPs) present among 731 SARS-CoV-2 PCR-positive hospitalized participants to *Biobanque québécoise de la COVID-19 (BQC19)*, with varying degrees of disease severity and times to intensive care unit (ICU) admission. In particular, one endophenotype, EP6, was associated with a greater proportion of ICU admission, mechanical ventilation, acute respiratory distress syndrome (ARDS) and death. Clinical features of this endophenotype showed increased levels of C-reactive protein, D-dimers, elevated neutrophils, and depleted lymphocytes. Moreover, metabolomic analysis supported a role for immuno-thrombosis in severe COVID-19 ARDS. Furthermore, Fibroblast Growth Factor Receptor (FGFR) and SH2-containing transforming protein 4 (SHC4) signaling were identified as molecular features associated with severe COVID-19. Importantly, a predictive model was developed and validated on an additional set of 631 SARS-CoV-2 PCR-positive patients to enable prediction of these endophenotypes, which reflect patients' likelihood of admission to ICU, solely based on clinical laboratory measurements. This suggests the use of blood markers as surrogates for generalizing these EPs to new patients and automating identification of high-risk groups in the clinic.

21 **Introduction**

22 The coronavirus disease 2019 (COVID-19) is a new human disease caused by the coronavirus
23 SARS-CoV-2 infection that has been assessed pandemic by the World Health Organization in
24 March 2020. As SARS-CoV-2 infection spread, a breath of outcomes of the infection became
25 apparent, from asymptomatic individuals to severely ill and dying, from complete recovery to
26 long-lasting symptoms (Marshall et al., 2020; Rubin, 2020). The emergence of novel diseases such
27 as COVID-19 presents the medical and scientific community with numerous challenges. Among
28 them, defining the molecular mechanisms of disease related to specific outcomes is important
29 to identify treatable traits and improve the performance of healthcare systems facing the
30 challenges brought by the pandemic.

31

32 Successfully reaching this precision medicine goal requires a more granular definition of the
33 pathology. A symptom-based method to discover molecular mechanisms of the disease may
34 result in a challenge emerging from the fact that the same higher-level phenomenon, such as
35 COVID-19 severity, can be produced by several different molecular mechanisms, a phenomenon
36 termed the «many-one» limitation (Hull, 1974). Recent advances in computing strategies, such
37 as machine learning, has enabled the development of methods that help overcome this limitation
38 by starting from molecular profiles instead of symptoms to define endophenotypes, *i.e.*
39 subgroups of individuals who are inapparent to traditional methods but share a common set of
40 molecular factors that can lead to treatable traits (Berrettini, 2005). Establishing successful
41 treatment strategies requires a tailored approach to the underlying molecular mechanisms that
42 can help predict and alter disease trajectories (Russell and Baillie, 2017). Endophenotypes can

43 become apparent using extensive molecular phenotyping combined with machine learning
44 algorithms (Blatti III et al., 2020; Emad et al., 2020; Te Pas et al., 2017). Current investigations of
45 endophenotypes in COVID-19 have mainly relied on supervised approaches using fixed outcomes
46 (such as disease severity) and integrating clinical variables at the onset (Al-Hadrawi et al., 2022).
47 We hypothesize that using an unsupervised approach exploiting a rich molecular dataset can
48 provide novel mechanistic insights into the pathobiology of severe COVID-19 that can help
49 physicians improve diagnosis and prognosis.
50
51 Therefore, this study aims to identify endophenotypes linked to diverse clinical trajectories of
52 COVID-19 using the extensive molecular phenotyping of a cohort of 731 SARS-CoV-2 positive
53 hospitalized patients from the *Biobanque québécoise de la COVID-19* (BQC19,
54 www.quebeccovidbiobank.ca) (Tremblay et al., 2021), a prospective observational cohort of
55 SARS-CoV-2 positive and negative participants recruited in the province of Québec, Canada, to
56 improve our understanding of COVID-19 pathobiology and our capacity to alter disease
57 outcomes.
58
59 In this manuscript, we report the identification of six endophenotypes in hospitalized SARS-CoV-
60 2 positive participants to BQC19, associated with different clinical trajectories. The molecular
61 information underpinning these endophenotypes was used to increase our understanding of
62 pathobiology and predict the likelihood of patients admitted to the hospital to be admitted to
63 the ICU using clinical blood workups.
64

Results

Unsupervised clustering of SARS-CoV-2-positive hospitalized BQC19 participants reveal endophenotypes associated with varying disease severity

In this study, we aimed to identify endophenotypes of COVID-19 based on the circulating proteome of patients in our cohort of SARS-CoV-2 positive hospitalized participants to BQC19 (n = 1,362, Table 1), using an unsupervised approach. Figure S1 shows the distribution of the time of hospital admission of the patients and the corresponding waves as defined by National Institute of Public Health of Quebec (https://www.inspq.qc.ca/covid-19). For this purpose, we performed consensus agglomerative clustering of the subset of patients (n = 731, Table S1) for whom data corresponding to circulating proteome measured by a multiplex SOMAmer affinity array (Somalogic, ~5,000 aptamers) (Gold et al., 2010) was available in BQC19. The remaining samples were kept aside for follow-up analysis. First, the optimal number of clusters (k = 6) was identified using two criteria, Akaike's Information Criteria (AIC) and Bayesian Information Criteria (BIC) (Figure 1A); then, consensus agglomerative clustering (Euclidean distance and Ward linkage) (Murtagh and Legendre, 2014; Ward Jr, 1963) using bootstrap subsampling was performed to obtain six robust clusters (see Methods for details) (Figure 1, Figures S2 and S3).

The clinical and pathological characteristics of patients in each endophenotype is provided in Table S1. To characterize the identified endophenotypes (EPs) with respect to disease severity, we performed two-sided Fisher's exact test to assess their enrichment (or depletion) in "severe" or "dead" outcome. EP6 was significantly enriched in the severe/dead outcomes (Benjamini-Hochberg false discovery rate (FDR) = 1.72E-18) with these outcomes observed in 66.1% of EP6

87 patients. Meanwhile, EP1 was significantly depleted in severe/dead outcomes (FDR = 8.23E-11)
88 (Figure 2A, Table S1) with these outcomes only observed in 11.6% of EP1 patients. In addition,
89 EP6 was enriched in participants 1) receiving oxygen therapy (FDR = 6.24E-12), 2) receiving
90 ventilatory support (FDR = 6.63E-12), and 3) being admitted to intensive care unit (ICU) (FDR=
91 1.26E-22) (Figure 2A, Table S1). Kaplan Meier analysis (Kaplan and Meier, 1958) also confirmed
92 that the identified EPs have a distinct temporal pattern of admission to ICU (multivariate logrank
93 test P = 5.06E-36), with EP1 (EP6) having the highest (lowest) chance of not being admitted to
94 ICU (or die prior to that) in a 40-day span since their admission to the hospital (Figure 2B). A
95 similar pattern can be observed when patients that died before admission to ICU were excluded
96 (Figure S4, multivariate logrank test P = 6.55E-36). A two-sided Mann-Whitney U (MWU) test
97 showed that patients in EP5 were generally older than other EPs (FDR = 6.94E-5), while EP3
98 included younger patients (FDR = 1.82E-4). However, EP6 (which had the most severe patients)
99 did not show enrichment in older patients or individuals with high BMI (two-sided MWU
100 FDR>0.05) (Figure 2C, Table S1).
101
102 These analyses revealed that the unsupervised approach was able to identify endophenotypes
103 with distinct disease characteristics and outcomes using the circulating proteome of the patients.
104 We identified EP6 as a group of participants with an increase in many measures of COVID-19
105 disease severity.
106
107 **EP6 is enriched with BQC19's participants having acute respiratory distress syndromes**

108 In accordance with increase disease severity, EP6 was also enriched in COVID-19 medical
109 complications (two-sided Fisher's exact test): acute respiratory distress syndrome (ARDS) (FDR =
110 1.43E-10), acute kidney injury (FDR = 6.37E-7), bacterial pneumonia (FDR=2.13E-6), liver
111 dysfunction (FDR = 9.32E-3), and hyperglycemia (FDR = 1.56E-2) (Figure 3, Table S2). The
112 frequency of ARDS was just below 8% in EP1 compared to greater than 44% in EP6, making this
113 complication a key feature of this cluster (Figure 3, Table S2).
114
115 **EP6 is enriched in blood metabolites associated with severe COVID-19.**
116 To further characterize each EP and gain insight into mechanisms of disease, metabolomic
117 profiling of plasma samples was done in parallel to the SOMAmer analysis. The results yielded
118 data on 1,435 metabolites, of which 576 were found significantly altered in EP6 (two-sided MWU
119 FDR < 0.01). Moreover, the metabolomic characterization of the plasma samples supported the
120 distinction in blood composition at the levels of metabolomic sub-pathways and individual
121 metabolites between the different EPs (Figure 4 and S3).
122
123 **Pathway enrichment analysis identifies FGFR-signaling in severe COVID-19 acute respiratory**
124 **distress syndrome**
125 To gain insight into the molecular mechanisms underlying the severity in EP6, we performed
126 pathway enrichment analysis using the Knowledge Engine for Genomics (KnowEnG) (Blatti III *et*
127 *al.*, 2020) for the aptamers associated with EP6. Since aptamers were used to identify the EPs, it
128 is expected that many of them would be significantly associated with the EPs. As a result, we
129 selected a very strict threshold of FDR < 1E-20 (two-sided MWU test) to identify top aptamers

130 associated with EP6 (Table S4). We then used the gene set characterization pipeline of KnowEnG
131 with Reactome (Gillespie et al., 2021) pathway collection. This analysis showed that while EP6 is
132 characterized by pathways associated with Interleukins and Cytokine Signaling in Immune
133 system, multiple instances linked it with Fibroblast Growth Factor Receptor (FGFR) signaling,
134 identifying this pathway as a potential driver of severe pathology that was not present in other
135 EPs (Tables 2 and S4).
136
137 **SHC4 genotype and protein expression levels are associated with higher odds of belonging to**
138 **EP6**
139 To further improve our understanding of the molecular mechanisms underlying EP6, we
140 leveraged an additional dataset of Genome Wide association Study (GWAS) corresponding to
141 these patients. We identified 25 single nucleotide variations (SNVs) distributed in 13 annotated
142 genes, that were below a p-value threshold of 1E-4 differentiating EP6 versus the rest (Table 3).
143 We then investigated each of the SNVs to which we could assign a gene and an aptamer, to assess
144 whether their protein product in circulation was differentially regulated by the genotype (Table
145 4). We discovered two genes, *SHC4* (encoding SHC adaptor protein 4) and *CACNA2D3* (encoding
146 calcium voltage-gated channel auxiliary subunit alpha2 delta3) for which there was a significant
147 association between genotype and protein expression levels (p-values < 0.05). While *CACNA2D3*
148 may have mild impact on EP6 membership (odd ratio = 0.61, Table 4), SHC4 was one of the top-
149 enriched aptamers (position 32 out of 4,985), with odds ratio of 11.98 and 2.00 for the protein
150 product and SNV, respectively of belonging to EP6 for the alternative allele. Therefore, the GWAS
151 analysis revealed that the signaling adaptor protein SHC4 may play an important mechanistic role

152 in contributing to severe disease pathology. To gain further insight into the potential role of SHC4,
153 we investigated the metabolites associated with SHC4 in EP6. The only significantly correlated
154 metabolite was 6-oxopiperidine-2-carboxylate (Spearman's rank correlation = 0.40, FDR = 0.012),
155 where the p-values were corrected for the number of metabolites using Benjamini-Hochberg
156 FDR.
157
158 **A predictive model based on blood markers predicts EPs in a separate validation cohort**
159 To further characterize each EP, we assessed the clinical laboratory results obtained from blood
160 draws and compared them between the groups. We focused on 21 markers that were measured
161 in at least 50% of the patients used for consensus clustering (Figure 5A and Table S5) and used
162 the summary value reported in the BQC19 database corresponding to the most extreme
163 measurement among multiple blood draws (Table S5 provides this information for each blood
164 marker). Figure 5A shows the elevation and depletion of these markers in the identified EPs. EP6
165 is characterized by abnormal values in markers of inflammation (lymphopenia, total white blood
166 cells count, neutrophilia, C-reactive protein (CRP)), liver damage (alanine aminotransferase (ALT),
167 albumin, lactate deshydrogenase (LDH)), blood clotting disorder (D-dimers, low hemoglobin,
168 International Normalized Ratio (INR) and hyperglycemia (glucose).
169
170 To identify relationships that may shed light on factors influencing clinical laboratory results
171 defining EP6, we also performed Spearman's rank correlation analyses between each blood test
172 values and metabolites (Table S5).
173

174 Since EPs and particularly EP6, which we identified as the EP with worst outcome, showed a clear
175 and distinct clinical laboratory result signature compared to other EPs, we sought to develop a
176 predictive model based on these signatures. Due to the presence of missing values for these
177 markers in our cohort, we developed a nearest-centroid classifier that is capable of dealing with
178 missing values and can predict EPs based on blood markers (see Methods for details). To test the
179 ability of this model on prediction of EPs on an independent yet similar dataset, we used data
180 corresponding to 631 SARS-CoV-2 positive hospitalized BQC19's participants that did not have
181 circulating proteome data and hence were not used to identify the endophenotypes. The clinical
182 and pathological characteristics of patients in each predicted endophenotype (PEP) is provided
183 in Figure 5B-5E and Table S6.
184
185 Our predictive model identified 116 of these patients to belong to EP6. Fisher's exact test showed
186 a significant enrichment of the predicted EP6 (PEP6) in severity/dead (FDR = 1.77E-22), while
187 PEP1 and PEP2 were significantly depleted in these outcomes (FDR = 1.61E-4 and FDR = 1.30E-8,
188 respectively), as shown in Figure 5B and Table S6. Similar to EP6, PEP6 was also significantly
189 enriched in participants 1) receiving oxygen therapy (FDR = 2.38E-8), 2) receiving ventilatory
190 support (FDR = 4.40E-8), and 3) being admitted to ICU (FDR = 1.23E-24) (Table S6). Kaplan Meier
191 analysis also confirmed that these PEPs have a distinct temporal pattern of admission to ICU
192 (multivariate logrank test P = 1.05E-34), with PEP6 having the lowest chance of not being
193 admitted to ICU (or die prior to that) in a 40-day span since their admission to the hospital (Figure
194 5E).
195

196 These results suggest that our predictive model can use these 21 blood markers to generalize the
197 definition of endophenotypes to patients for whom the proteome data is unavailable.
198
199 **Discussion**
200 The results presented herein came from the unsupervised clustering of the circulating proteome
201 from a large cohort of deeply-phenotyped SARS-CoV-2 positive hospitalized participants, that
202 provided both expected and novel findings into the molecular mechanisms regulating COVID-19.
203 They led to the identification of six endophenotypes with different clinical trajectories and
204 distinguishing characteristics summarized in Table 5. One endophenotype, (EP6) was associated
205 with worst clinical outcome of COVID-19 (enriched in acute respiratory distress syndrome)
206 reflected by a greater proportion of ICU admission, mechanical ventilation, and severe/death
207 outcomes (Figure 1). Clinical features of this endophenotype were consistent with published
208 literature with increased levels of CRP, D-dimers, elevated neutrophils, and depleted
209 lymphocytes (Figure 5A, Table S5). Our approach enabled the identification of interleukins, FGFR
210 and SHC4 signaling as cardinal features of the molecular pathways associated with severe COVID-
211 19. Importantly, this information was sufficient to train an accurate predictive model that could
212 in the near future support clinical care, since it only requires data from routine clinical laboratory
213 results for prognosis.
214
215 *The approach: unsupervised clustering capacity at identifying clinically meaningful*
216 *subpopulation*s

217 Our unsupervised clustering approach in conjunction with a rich molecular dataset enabled us to
218 identify endophenotypes that could not be captured using traditional methods classifying the
219 population in two bins solely based on severity. This is in part because of the «many-one»
220 limitation: the same higher-level phenomenon (COVID-19 severity) can be produced by several
221 different molecular mechanisms. Determining endophenotypes using an unsupervised method
222 provides a higher granularity and increases the chance to identify distinct molecular mechanisms
223 and pathways resulting in similar COVID-19 severity. Accordingly, we identified two
224 endophenotypes with more favorable outcomes (EP1 and EP2), three endophenotypes with
225 intermediate outcomes in terms of severity (EP3, EP4 and EP5) and one endophenotype which
226 led to worst outcomes compared to all others (EP6).
227
228 The identification of endophenotypes was done systematically using robust consensus clustering
229 of aptamer expression levels in which the optimum number of clusters was determined
230 congruently using two well-established measures: AIC and BIC. The consensus clustering using
231 bootstrap sampling (1000 times) ensured identification of robust clusters that are not sensitive
232 to exclusion of some of the samples (20% randomly selected and excluded at each cycle).
233 Moreover, identifying the best number of clusters using AIC/BIC (both of which agreed with each
234 other) allowed us to reveal the patterns of the EPs directly from the data, instead of imposing a
235 pattern onto it through human supervision. This is an important strength of the study that
236 enabled us to identify distinct molecular patterns of patients that could have remained
237 undetected using other traditional approaches.
238

239 Moreover, to improve the translational applicability of EPs, we developed a predictive model
240 based only on laboratory measured blood markers to generalize the definition of these
241 endophenotypes to unseen samples without measured aptamer expression levels.
242 Characteristics of EPs predicted solely based on their blood markers were consistent with the
243 original EPs, suggesting the use of blood markers as surrogates for generalizing these EPs to new
244 patients and automating identification of high-risk groups in the clinic. This approach takes into
245 account the effect of multiple blood variables simultaneously and incorporates the full
246 distribution of each variable. This is in contrast to the clinical laboratory results that are
247 automatically flagged as within or outside normal range, one variable at a time, therefore
248 increasing the clinical applicability of our model by leveraging a wider spectrum of information
249 to prognose patient outcome.
250
251 *COVID-19 molecular pathology*
252 The datasets used in this study carry rich molecular information on mechanisms of disease for
253 COVID-19. EP6 is characterized by its enrichment in ARDS (44% vs 8% in EP1, Figure 3), acute
254 kidney injury (45%) and liver dysfunction (19%) (Table S2). Low levels of Sphingosine 1-phosphate
255 (S1P) are associated with ARDS and were shown to be associated with greater ICU admission and
256 decrease survival in COVID-19 (Marfia et al., 2021). Accordingly, we found that S1P levels are
257 depleted in EP6 while they are enriched in EP1 (Figure 4A). Interestingly, the aptamers detecting
258 neutral ceramidase, an enzyme converting ceramides into sphingosine, is enriched in EP1
259 (although changes in protein abundance as detected by aptamers may not necessarily reflect
260 changes in enzymatic activity). Accordingly, dihydroceramides and ceramides are depleted in

261 cluster EP1. Conversely, dihydroceramides and ceramides are significantly enriched in EP6,
262 suggesting that there is a shunting of the pathway away from sphingosine towards more pro-
263 inflammatory ceramides in EP6 associated with metabolic disorders (Lachkar et al., 2021).
264 Moreover, one of the top aptamers found enriched in EP6, is the enzyme Serine
265 palmitoyltransferase 2 (SPTLC2) (Table S4) (Han et al., 2009; Lone et al., 2020). These results
266 suggest a counterbalance between ceramides and sphingosine, where the former is associated
267 with poorer outcomes during critical illness, whereas higher levels of the latter is associated with
268 more favorable outcomes in ARDS.
269
270 *Metabolomic profile of EP6 supports a role for immuno-thrombosis-mediated organ damage in*
271 *COVID-19*
272 To obtain a more comprehensive understanding of the alteration in metabolic profiles in EP6, we
273 investigated which metabolic sub-pathways were significantly enriched in EP6 (Figure 4, Table
274 S3). The two top pathways (FDR < 1E-2) are "Methionine, Cysteine, SAM and Taurine
275 Metabolism" and "phosphatidinylethanolamine (PE)". Interestingly, these two pathways are
276 known to interact (Blachier et al., 2020), with PE methylation a major consumer of S-
277 Adenosylmethionine (SAM) leading to the synthesis of S-Adenosylhomocysteine (SAH) and
278 cystathionine (Ye et al., 2017), which itself has been found upstream of 2-hydroxybutyrate and
279 2-aminobutyrate in a model of hepatoxicity (Parman et al., 2011). SAH, cysthathionine, 2-
280 hydroxybutyrate and 2-aminobutyrate are significantly enriched in EP6. Congruently, EP6 is
281 enriched (FDR < 1E-2) in liver dysfunction (Figure 3, Table S2), with markers of liver dysfunction

282 all significantly altered in clinical blood works: ALT, albumin, bilirubin and LDH (Figure 5A, Table
283 S5).
284
285 PEs become exposed at the surface of cell membranes upon exposure to stress, inflammation,
286 and cell death (Ran et al., 2002; Stafford and Thorpe, 2011). In a Syrian hamster model, infection
287 with SARS-CoV-2 had markedly increased PE expression in the animals that were fed a high salt,
288 high fat diet, demonstrating the interaction between infection and metabolic disorder with the
289 abundance of circulating PE (Port et al., 2021). Phospholipids-containing microparticles from
290 platelet activation contribute to Tissue Factor activation and pro-thrombinase activity (Ataga,
291 2009). Platelets-derived microparticles have a much greater procoagulant activity than activated
292 platelets (Sinauridze et al., 2007). Exposure of glycerophospholipids in conjunction with
293 phosphatidinylserine (PS) enhances factor X activation and increases pro-thrombinase activities
294 (Majumder et al., 2011; Tavoosi et al., 2011). Interestingly, red blood cells exposed to paclitaxel,
295 PS were exposed to the surface by protein kinase C (PKC) zeta activation of scramblase (Kim et
296 al., 2018). The aptamer detecting PKC zeta is one of the top aptamers associated with EP6 (Table
297 S4). PKC zeta can be activated by testosterone, Dehydroepiandrosterone(DHEA) (Sato et al.,
298 2008) and dexamethasone (Kajita et al., 2001), signals of relevance to EP6. The membranes of
299 azurophilic granules, which contains Cathepsin G representing the most enriched aptamer in EP6,
300 are enriched in PE relative to PC (MacDonald and Sprecher, 1989). Accordingly, EP6 in addition
301 to significantly enhanced PE abundance, showed decrease platelets count, increased D-Dimers,
302 INR and activated partial thromboplastin time (aPTT) (Figure 5A, Table S5), hallmarks of
303 Disseminated Intravascular Coagulation (DIC), a serious and often lethal complication of sepsis

304 (Papageorgiou et al., 2018). Liver lesions are frequently observed in DIC (Esaki et al., 1984), where
305 liver damage can cause DIC, or exacerbate its manifestation due to its function in clearing
306 activated products of the coagulation cascade. Taken together, the metabolomic profile of EP6
307 supports pro-coagulation activity in circulation that can be linked to organ damage.
308
309 Many early reports suggested a role for immunothrombosis involving neutrophil-mediated
310 release of NETs contributing to endothelial dysfunction as a mechanism of microthrombosis in
311 COVID-19 associated ARDS (Barnes et al., 2020; Bonaventura et al., 2021; Ding et al., 2021). These
312 findings have been supported by several studies carried out in humans (Blasco et al., 2021;
313 Desilles et al., 2022; Englert et al., 2021; Leppkes et al., 2020; Middleton et al., 2020; Obermayer
314 et al., 2021; Ouwendijk et al., 2021; Petito et al., 2021; Skendros et al., 2020). All of these studies
315 were performed with 7 to 77 participants. Our study supports these findings in two important
316 ways: 1) we used a much greater sample size (n = 731) and, 2) the identification of molecular
317 factors associated with immuno-thrombosis emerged from an *unsupervised* analysis of deep
318 phenotyping of the participant population. The strength of the extensive characterization
319 performed in this study has enabled the finer definition of molecular mechanisms of disease by
320 providing associations between the circulating proteome, metabolome and clinical laboratories
321 results.
322
323 *Tryptophan and polyamine metabolisms in COVID-19 acute kidney injury*
324 SARS-CoV-2 infection has been shown to be associated with altered kynurenin levels associated
325 with increased IL-6 and kidney injury (Thomas et al., 2020). Interestingly, we also observed

326 Kynurenin to be enriched in EP6 but depleted in EP1, supporting the association of increased
327 kynurenin with COVID-19 severity and the enrichment in acute kidney injury complication.
328 Spermidine/spermine N(1)-acetyltransferase (SSAT) contributes to polyamine synthesis. In
329 addition, its extracellular metabolite, N1,N12-diacetylspermine, is one of the top 15 metabolites
330 enriched in EP6 (Figure 4A), is positively correlated with Urea and creatinine, and is negatively
331 correlated with lymphocyte numbers (Table S5). Deletion of SSAT in mice is protective against
332 LPS-induced kidney injury (Zahedi et al., 2010). SSAT activity is associated with white blood cell
333 count in Acute Myeloid Leukemia and Chronic Myeloid Leukemia patients (Pirnes-Karhu et al.,
334 2014). This suggests that the tryptophan and polyamine metabolisms are associated with acute
335 kidney injury in COVID-19 and identifies potential pathways of disease progression.
336
337 *Novel molecular markers of COVID-19 pathology: FGFR and SHC4*
338 Two of the outstanding novel molecular factors associated with COVID-19 ARDS identified by our
339 study are FGFR and SHC4. Circulating levels of the pro-angiogenic FGF-2 has been associated with
340 COVID-19 severity and creatine levels in a study of 208 SARS-CoV-2 positive participants (Smadja
341 et al., 2021). It is noteworthy that the use of Nintedanib, an inhibitor of FGFR, Vascular
342 Endothelial Growth Factor Receptor (VEGFR) and Platelet-Derived Growth Factor Receptor
343 (PDGF-R) approved for use in interstitial lung disease, improved pulmonary inflammation and
344 helped wean off mechanical ventilation of three middle-aged obese COVID-19 patients where
345 lung function restoration has been challenging (Bussolari et al., 2021). While the adaptor protein
346 SHC4 has not been experimentally demonstrated to modulate FGFR signaling, a 12-gene
347 biomarker signature associated with melanoma contains FGFR2, FGFR3 and SHC4 (Liu et al.,

348 2013). It is attractive to speculate that SHC4 may act downstream of FGFR or other associated
349 growth factor receptors, favoring immuno-thrombosis associated with COVID-19 ARDS. In view
350 of the limited knowledge of this understudied member of the SHC family, we looked at the
351 metabolites correlated with SHC4 to gain insights into its possible functions. Interestingly, 6-
352 oxopiperidine-2-carboxylate (the only significantly correlated metabolite to SHC4 in EP6) was
353 found to be negatively associated with glomerular filtration rate in a GWAS study of kidney
354 disease and hypertension in African-Americans (Luo et al., 2021). Acute kidney injury is a frequent
355 complication of acute liver failure (Agarwal et al., 2013) and liver dysfunction is associated with
356 abnormal coagulation (Williams et al., 1993). The overall molecular information coming from the
357 multi-modal analysis of EP6 points to a triad between liver function, kidney function and
358 hemostasis that becomes dysfunctional following ARDS-associated immuno-thrombosis.
359 Whether the presence of SHC4 in circulation is a marker of dysfunction of this triad, or an active
360 actor immuno-thrombosis remains to be determined. Moreover, the identity of the cells
361 expressing SHC4, leading to its presence in the circulation is not known. Taken together, our
362 identification of FGFR and SHC4 signaling pathways distinguishing EP6 from other
363 endophenotypes, supports further investigation of antagonists of those pathways to treat severe
364 manifestations of COVID-19 and their potential use as biomarkers of severe disease activity.
365
366 *Limitations and considerations*
367 The data presented in this study come from individuals participating to BQC19, a prospective
368 observational cohort built to study COVID-19 in Québec (Canada) with its specific population
369 profile as reported previously (Tremblay *et al.*, 2021). While the number of participants was

370 sufficient to establish the endophenotypes using the extensive proteomic profile available in
371 BQC19, it was insufficient for traditional genome-wide association study (GWAS) to identify
372 relations between SNVs and the identified endophenotypes (Zhou et al., 2021). Instead, we
373 exploited the top SNVs that distinguished EP6 from other EPs in a pQTL analysis. Because these
374 results show a potential genetic functional causality, it gives us the confidence that these
375 associations are likely not due to random chance; however, the robustness of this approach
376 needs to be further tested in other studies. A chronological bias may also be present, as most of
377 the participants used for endophenotyping in this study were recruited during the first two waves
378 of the pandemic (Figure S1), prior to widespread vaccination in Québec and prior to the
379 appearance of the Omicron variant and sub-variants. Therefore, some of the features of the
380 identified endophenotypes may change over the course of the pandemic. It will be essential to
381 continue to assess the molecular profiles longitudinally to better understand the dynamic nature
382 of host-pathogen interactions. It will also be interesting to compare the profiles of COVID-19
383 ARDS to other viral-induced ARDS, to identify commonalities as well as distinguishing features.
384
385 In this study, we used circulating proteome as determined by aptamers to identify
386 endophenotypes, a task for which it is well suited as it can capture a dynamic landscape.
387 However, several important considerations need to be mentioned. First, raw (unnormalized)
388 expression values of the same aptamer can be used to compare different samples, but these
389 values cannot be used to compare different aptamers against each other in the same sample,
390 since they only show the relative abundance of expression and not absolute expression. As such,
391 one needs to first normalize these values across samples (one aptamer at a time) and then

392 subject them to follow-up analysis such as clustering, an approach that we adopted in this study.
393 Second, since information only shows relative abundance, focusing on an individual aptamer and
394 analyzing it will require additional measurements to establish absolute abundance. Moreover, if
395 one wants to analyze aptamers individually (instead of the collective approach that we used in
396 this study), they need to consider the effect of complexes and non-specific binding that may
397 result in noisy data. As such, we suggest that the aptamer expression data be used collectively
398 and after proper normalization, which enabled us to identify various EPs and important molecular
399 mechanisms discussed in this study.
400
401 In this work, we developed a predictive model based on blood markers that enables us to
402 generalize the definition of EPs to scenarios where data on circulating proteome is not available.
403 This significantly increases the applicability of this approach and may enable automating
404 identification of high-risk individuals in the clinic. However, time and follow-up studies are
405 required to move this predictive model and the definitions of EPs from research to clinic and
406 develop it as an acceptable clinical practice. Nonetheless, our approach can be used to study
407 COVID-19 in different cohorts and identify characteristics that can guide the treatment of the
408 disease.
409
410 *Future directions*
411 There is enormous amount of data within this study and BQC19 that can and should be exploited
412 by the scientific and medical community to improve our understating of COVID-19 and novel
413 emerging acute respiratory illnesses. Analyzing in more details the molecular profiles of the other

414 EPs, in particular EP3-5, which led to similar outcomes from distinct molecular pathways (Table
415 5) should further yield important insights into mechanisms of the disease. For example, EP5 is
416 enriched in males and cardiovascular disease complications, while EP4 is enriched in female (like
417 EP1) but with different distinct clinical trajectories pointing to sex-dependent and independent
418 molecular mechanisms of disease.
419
420 **Conclusion**
421 The major strength of this study is its starting point: unsupervised analysis of a large and deeply
422 phenotyped cohort. We showed that this approach can address both fundamental scientific
423 questions pertaining to mechanisms of disease and help the medical community improve patient
424 outcomes through early identification of patient that may follow a severe clinical course during
425 COVID-19.
426
427 **Methods:**
428 **Datasets and preprocessing**
429 The Biobanque québécoise de la COVID-19 (BQC19; www.quebeccovidbiobank.ca) is aimed at
430 coordinating the collection of patients' data and samples for COVID-19 related research. Data
431 and samples were collected from ten sites across the province of Québec (Canada) (Tremblay *et*
432 *al.*, 2021). BQC19 organizes the collected data, including clinical information and multi-omics
433 experimental data, before making it available in successive releases. For this study, we used
434 release #5 of the clinical data published in December 2021, the circulating proteome determined
435 using SOMAmers (Zhou *et al.*, 2021) and Metabolomics data (Ford et al., 2020). BQC19 GWAS

436 imputation data was generated by Tomoko Nakanishi at Brent Richards lab, Jewish General
437 Hospital and McGill University. Detailed codes used for generating the data can be found in:
438 https://github.com/richardslab/BQC19_genotype_pipeline
439
440 Our main corpus of analysis consisted of n = 1,362 hospitalized and SARS-CoV-2 positive patients
441 (based on qRT-PCR) of BQC19. This included n = 731 patients for which both clinical and
442 proteomic data were available as well as n = 631 patients for which proteomic data was not
443 available, but their clinical data contained measurements for more than half (at least 11 out of
444 21) of the blood markers that we used as a validation set for the predictive model developed in
445 this study.
446
447 We also obtained data (n = 731) corresponding to the circulating proteome measured between
448 April 2, 2020 and April 20, 2021 by a multiplex SOMAmer affinity array (Somalogic, 4,985
449 aptamers) from BQC19 (release #3 Sep. 2021, associated patients' data updated in release #5
450 Dec. 2021). When measurements of the same patients but at different time points were
451 available, we used the one corresponding to the first time point. SomaScan is a biotechnological
452 protocol commercialized by the Somalogic company. It relies on a set of artificial aptamers linked
453 to a fluorophore and each designed to bind a single protein. Once added to the sample, the
454 activity of each aptamer is measured through fluorescence and used to approximate the
455 expression level of the targeted protein. SomaScan protocol comprises several levels of
456 calibration and normalization to correct technical biases (Gold *et al.*, 2010). Log2 and Z-score
457 normalization were performed on each aptamer separately in addition to the manufacturer's

458 provided normalized data (hybridization control normalization, intraplate median signal
459 normalization, and median signal normalization). Since the data was analyzed by Somalogic in
460 two separate batches, we applied the z-score transformation separately to each batch, to reduce
461 batch effects. These additional transformations ensure that the measured values of different
462 aptamers are comparable and can be used in cluster analysis.
463
464 We obtained metabolomic data (1,435 metabolites) from BQC19. We used the batch-normalized,
465 missing values imputed and log-transformed version of the data.
466
467 **Analyses of the GWAS dataset**
468 For the GWAS analyses, annotation of SNVs were done using the biomaRt package (Durinck et
469 al., 2009) from R (R Core Team, 2022) and all analyses were done using R version 4.1.3. Quality
470 control steps were derived in majority from a 2017 QC tutorial article (Marees et al., 2018). At
471 the beginning, we had 867,450 markers and 2,429 samples. We import Plink format data into R
472 using the "read_plink" function from genio package (Ochoa, 2022) from R. We removed 103,592
473 non ACGT bi-allelic markers. We calculated the predicted sex by looking at the rate of
474 homozygote markers on chromosome 23. We removed 3,588 markers with call rates < 98%,
475 448,932 monomorphic markers and markers with MAF <0.05, and 28,092 markers with Hardy
476 Weinberg equilibrium < 1E-6 (calculated by the "HWE.exact" function from the genetics package
477 (Warnes et al., 2021) from R. For the EP6 cluster group analyses, we removed in addition 1,747
478 samples that were not in the cluster analysis, 8 samples with a sex discrepancy (based on
479 predicted sex calculated earlier and reported sex), and 3 samples with a heterozygosity rate > 3

480 standard deviations. We finally removed a pair of samples who had approximately the same
481 genome probably due to an error of manipulation. We couldn't know which one was the right
482 sample, so we removed both of them. We also had 2 pairs of individuals who had a pi-hat of ~0.5
483 (meaning first degree relatives), we decided to keep one sample per pair, the one with the higher
484 call rate. All other pairs of individuals had a pi-hat < 0.21 that is judge acceptable considering our
485 population. Pi-hat were calculated with the "snpgdsIBDMoM" function from SNPRelate package
486 (Zheng et al., 2012) from R. At the end of quality controls, 283,246 markers on 655 samples have
487 been used to perform association analyses.
488
489 To perform the principal component analyses (PCA), we took a subsample of independent
490 markers (pruning) with a maximum sliding window of 500,000 base pairs and a linkage
491 disequilibrium (LD) threshold of 0.2 using the "snpgdsLDpruning" function from the SNPRelate
492 package from R. We ran the PCA with the "snpgdsPCA" function from SNPRelate package from
493 R. The first 2 principal components (PCs) were considered significant.
494
495 For the GWAS analyses of the 283,246 remaining markers between EP6 cluster compared to all
496 others, we modeled a logistic regression with the dichotomous variable indicating if the
497 participants belong to the EP6 cluster as the outcome variable. We used the additive model for
498 markers as an independent variable and we adjusted the models with the first two PCs. Odds
499 ratio and p-values were calculated on each model. QQ-plots have been performed as quality
500 control of the models; p-values were plotted using "qqplot.pvalues" function from gaston
501 package (Perdry and Dandine-Roulland, 2020) from R (data not shown). We compared the

502 aptamers' normalized level of expression (based on normalization described earlier) between the
503 three groups of genotypes for each studied genes by performing standard ANOVA analyses
504 followed by Tukey *post hoc* tests (referred to in this study as pQTL analysis). Since aptamers
505 tested are limited compared to the SNVs, we have fixed significance p-values threshold below
506 1E-4 to report more SNVs instead of the more common 1E-5 suggestive threshold. Finally, to
507 identify if the cluster EP6 may be explained by the aptamers and the SNVs, we performed
508 multiple logistic regression analyses models include aptamers expression values, SNV genotypes
509 (additive model) and the two principal components. OR are reported with 95% confidence
510 intervals.
511
512 **Consensus agglomerative clustering**
513 Patients were clustered using agglomerative clustering, with Euclidean distance and Ward's
514 linkage (Murtagh and Legendre, 2014; Ward Jr, 1963). To identify number of clusters k, we used
515 the elbow method based on the Akaike Information Criterion (AIC) and Bayesian Information
516 Criterion (BIC). More specifically, we calculated the AIC and BIC for clustering using k = 2, 3, …, 20
517 and used the Kneedle algorithm (Satopaa et al., 2011) to identify the value of k corresponding to
518 the "elbow", where increasing the value of k does not provide much better modeling of the data.
519 Kneedle identified k = 6 as the number of clusters based on both AIC and BIC (Figure 1A).
520
521 Given the number of clusters in the data, we then used consensus clustering with sub-sampling
522 to obtain robust endophenotypes. We randomly sampled 80% of the patients 1000 times. Each
523 time, we used agglomerative clustering above with k = 6 to identify clusters. Given these 1000

524 clusterings, we calculated the frequency of two patients appearing in the same cluster, when
525 both were present in the randomly formed dataset. We then performed one final agglomerative
526 clustering of these frequency scores to identify the six endophenotypes (Figure S2A and Figure
527 1B). The distribution of Rand-Index, showing the concordance between each one of the 1000
528 clusterings and the final consensus clustering is provided in Figure S2B (mean Rand-Index =
529 0.823), reflecting a high degree of consistency.
530
531 **Metabolomic pathway characterization of EP6**
532 The 1435 metabolites measured were organized into 122 sub-pathways in the original dataset
533 (denoted as "SUB_PATHWAYS"). We first identified metabolites whose values were significantly
534 higher or lower in EP6 compared to other EPs (two-sided MWU test, FDR<0.01). Then, we used
535 these metabolites to perform pathway enrichment analysis (one-sided Fisher's exact test) based
536 on 122 pathways. The resulting p-values (Table S3) were then corrected for multiple tests using
537 Benjamini-Hochberg FDR.
538
539 **Nearest-centroid predictor based on blood markers**
540 In order to predict endophenotypes from blood tests, we developed a missing-value resilient
541 nearest-centroid classifier. We used the set of patients that were used to form the original EPs
542 (n = 731) as the training set and the set of patients that did not have proteome data as the
543 validation set (n = 631). First, we z-score normalized each blood marker across all the patients in
544 the training set, one marker at a time. We then formed a blood marker signature (a vector of

length 21) for each EP. Each element of an EP's signature corresponds to the mean of the corresponding marker across all patients of that EP.

To predict the EP label of each patient in the test set, we first z-score normalized their blood marker measurements using the mean and standard deviation of the blood markers calculated from the training set. Then, we calculated the cosine distance between each test patient's blood marker profile and the centroids (excluding missing values) and identified the nearest EP as the predicted EP (PEP) label of the patient.

Acknowledgements

This work was made possible through open sharing of data and samples from the Biobanque québécoise de la COVID-19, funded by the Fonds de recherche du Québec - Santé, Génome Québec, the Public Health Agency of Canada and, as of March 2022, the Ministère de la Santé et des Services Sociaux du Québec. We thank all participants to BQC19 for their contribution. This study was supported by the Fonds de recherche du Québec - Santé (FRQS)- Cardiometabolic Health, Diabetes and Obesity Research Network (CMDO)- Initiative. This work was also supported by Natural Sciences and Engineering Research Council of Canada (NSERC) grant RGPIN-2019-04460 (AE).

Permissions

The study was approved by the Institutional Ethics Review Board of the “Centre intégré universitaire de santé et de services sociaux du Saguenay-Lac-Saint-Jean” (CIUSSS-SLSJ) affiliated to Université de Sherbrooke [protocol #2021-369, 2021-014 CMDO – COVID19].

Figures

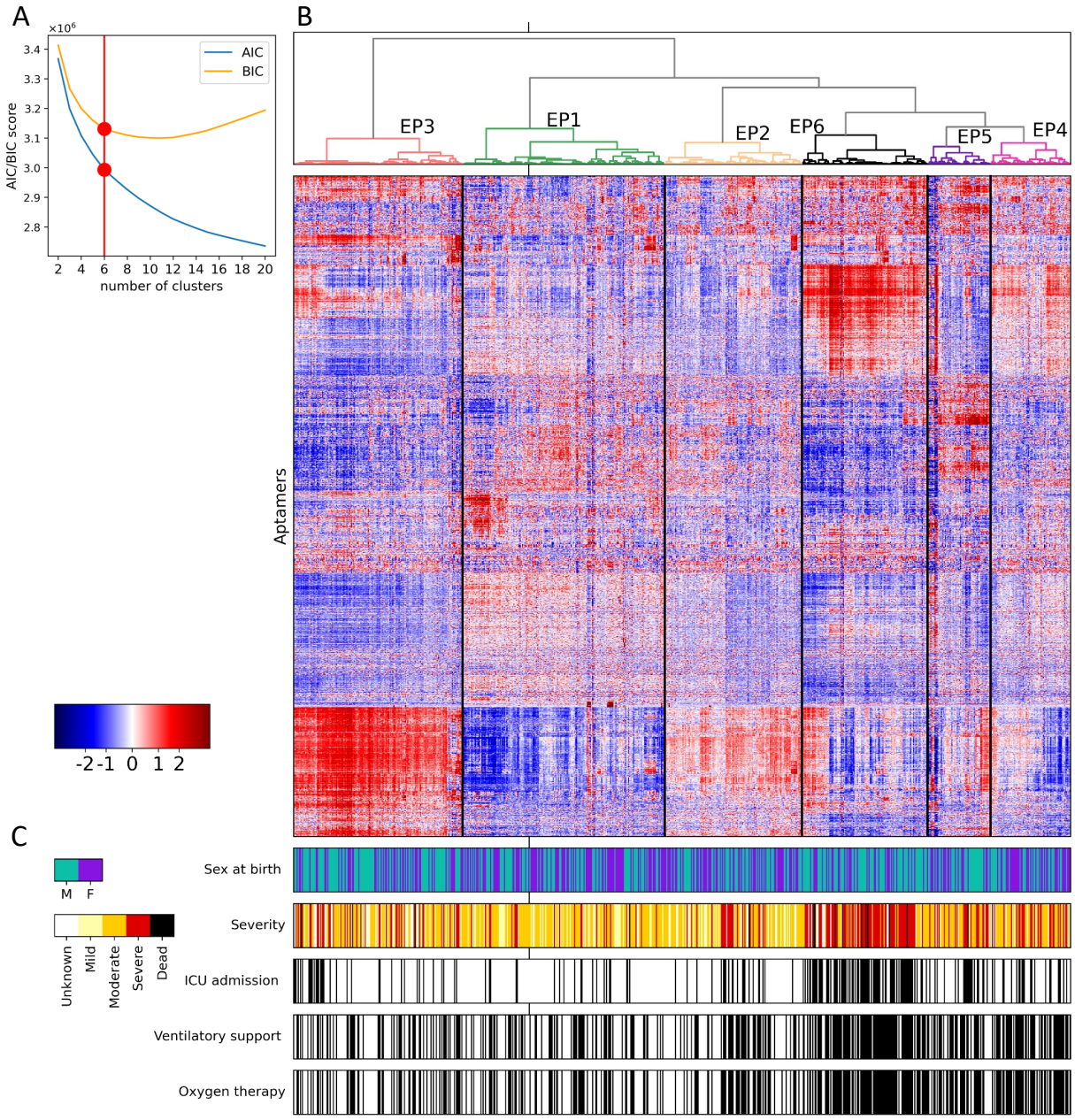

Figure 1: Unsupervised consensus clustering of SARS-CoV-2 positive patients. A) The elbow points (circles in red) of Akaike's Information Criteria (AIC) and Bayesian Information Criteria (BIC) curves versus number of clusters consistently corresponded to k=6 as the optimal number of clusters. B) The heatmap shows the expression of aptamers (rows) in each sample (columns). The dendogram shows the identified endophenotypes. C) Characterization of samples based on sex at birth, highest world health organization (WHO) severity level achieved, intensive care unit (ICU) admission, ventilatory support, and oxygen therapy. For the last three rows, a sample colored “black” reflects a label of “yes”.

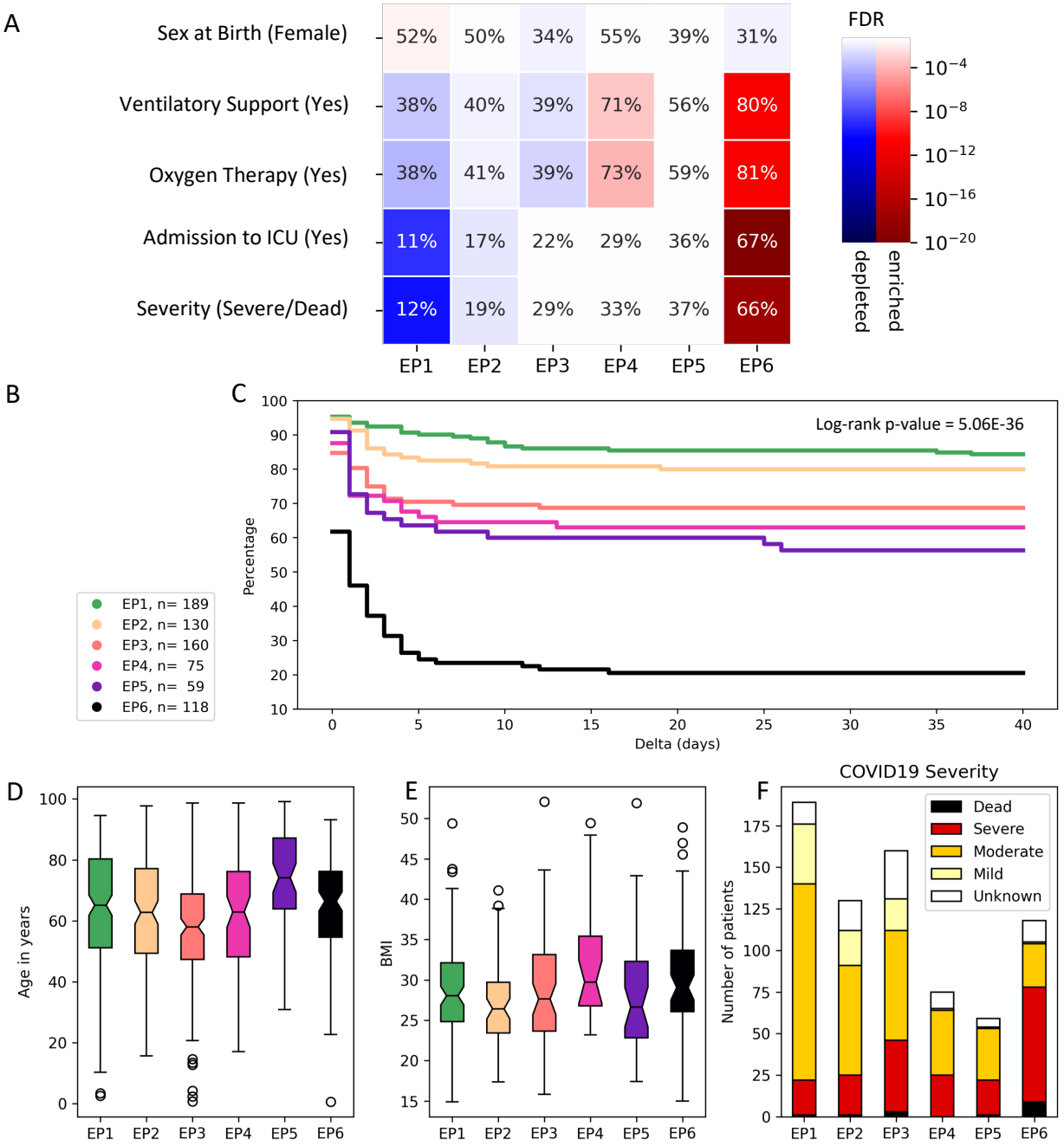

Figure 2: Characterization of endophenotypes (EPs).
A) Enrichment or depletion of each EP in clinical variables (one cluster versus rest). Two-sided Fisher's exact tests are used to calculate the p-values, which are corrected for multiple tests using Benjamini-Hochberg false discovery rate (FDR). Gradients of blue show depletion, while gradients of red show enrichment. FDR values above 0.05 are depicted as white. B) The number of patients in each EP and the colors used to represent them in panels C, D, and E. C) Kaplan-Meier analysis of the time between patients' admission to the hospital and their admission to intensive care unit (ICU) (or death if earlier) for each EP (Delta). D) Distribution of age in each EP. E) Distribution of BMI in each EP. F) COVID-19 severity in each EP.

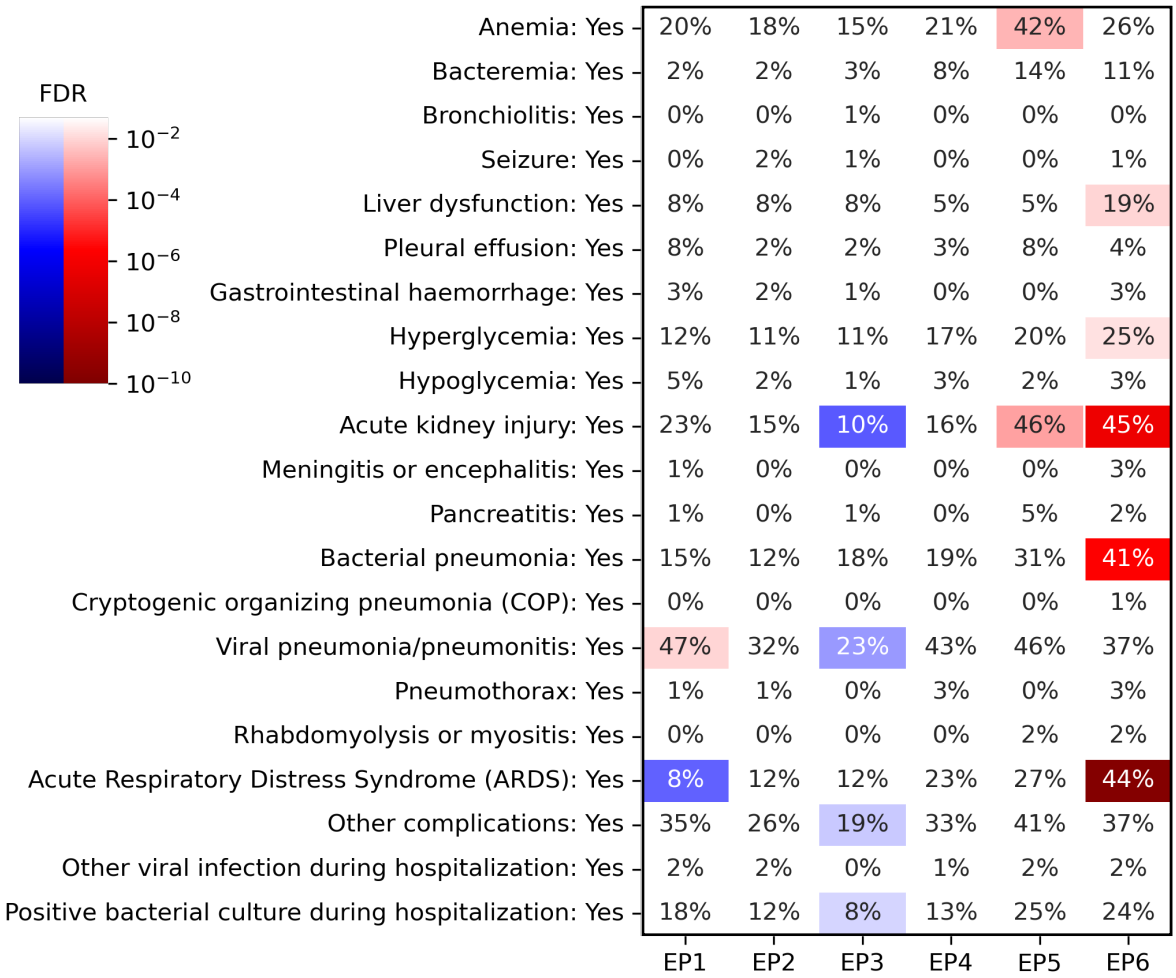

Figure 3: Frequency and significance of complications in different EPs.
The value in each cell shows the percentage of patients of that EP (column) that suffered from the complication (row). The colors represent two-sided Fisher's exact test false discovery rate (FDR, corrected for multiple tests). Red represents enrichment, while blue represents depletion. FDR values below 0.05 are shown as white.

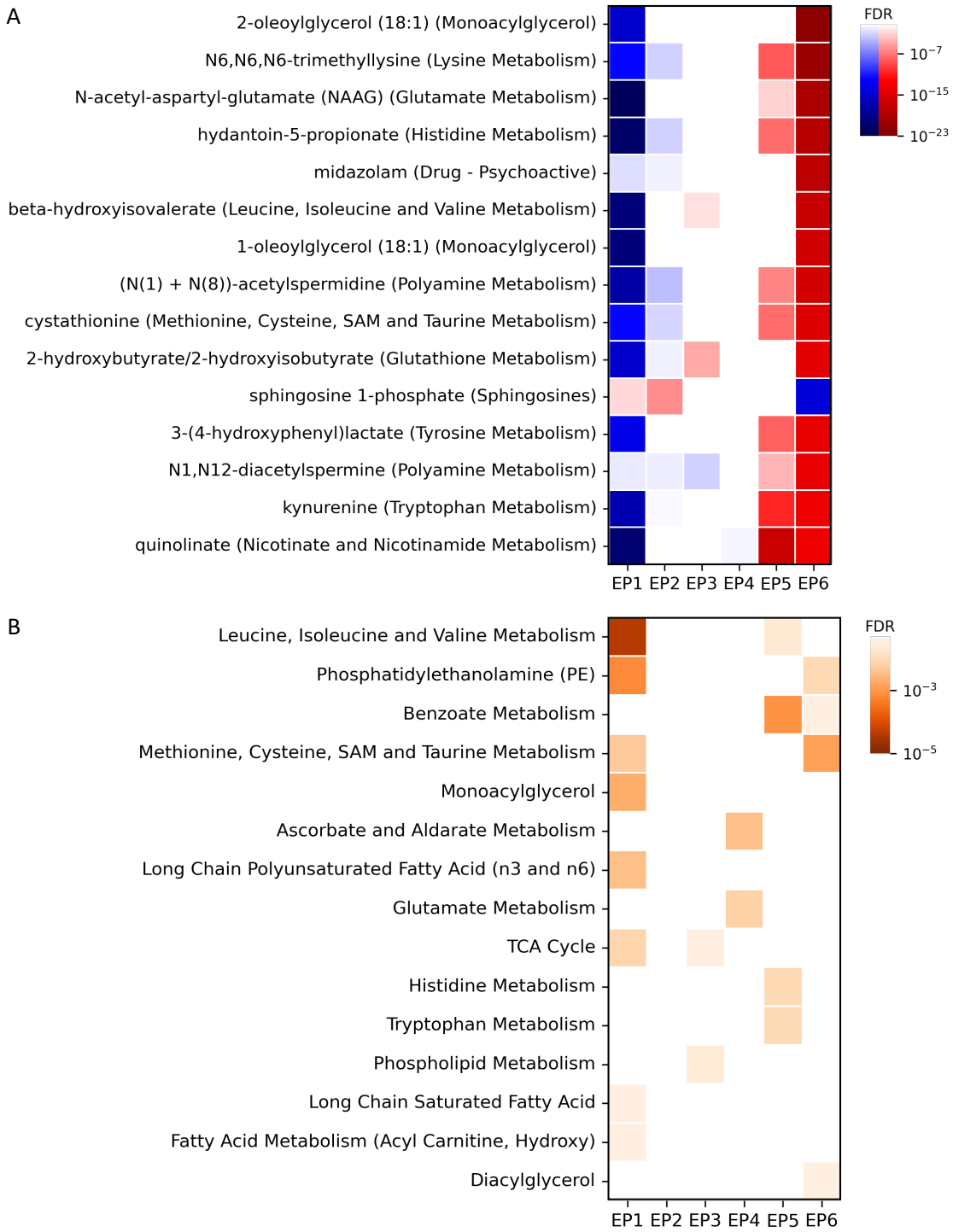

Figure 4: Metabolite characteristics of endophenotypes (EPs).
A) The heatmap shows the over-expression (red) and under-expression (blue) of metabolites in different EPs (two-sided Mann–Whitney U test). Row names show metabolites followed by the sub-pathway to which they belong in parentheses. Only top 15 metabolites (based on false discovery rate for EP6) for which a definite name and sub-pathway was available are shown. Full list is provided in Table S3. B) The heatmap shows the enrichment (one-sided Fisher's exact test) of EPs in different metabolite sub-pathways. See Table S3 for the full list.

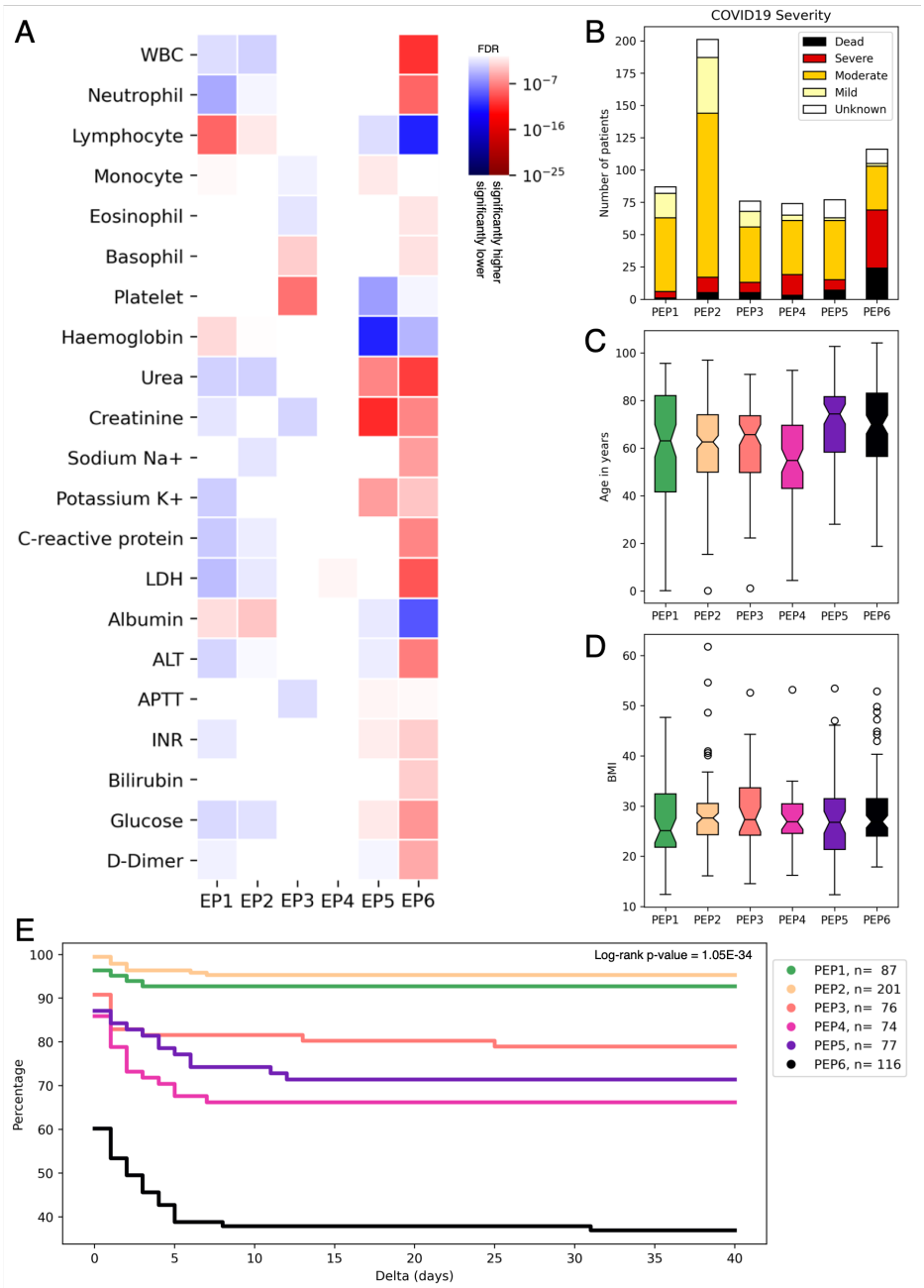

Figure 5: Differential expression patterns of blood markers in the identified endophenotypes (EPs) and characterization of predicted endophenotypes (PEPs) based on the predictive model. A) Heatmaps of false discovery rates (FDR) values for two-sided one-vs-rest Mann–Whitney U tests for 21 blood markers for each EP. Abbreviations used: WBC = white blood cells, LDH = lactate deshydrogenase, ALT = alanine aminotransferase, aPTT = activated partial thromboplastin time, INR = International Normalized Ratio. FDR values below 0.05 are shown as white. B) World health organization COVID-19 severity assessed in each PEP. C) Distribution of age in each PEP. D) Distribution of BMI in each PEP. E) Kaplan-Meier analysis of the time between patients' admission to the hospital and their admission to ICU (or death if earlier) for each PEP (Delta). The colormap

612 in panel E shows the number of patients in each PEP group and the colors used to represent them
613 in panels C, D, and E. PEPs were predicted based on blood markers and were not used to originally
614 identify the EPs.

615 **Tables**

616 **Table 1:** Clinical and pathological characteristics of the BQC19's participants used in this study.

		Cohort (n = 1,362) No. (%)
Age in years	<45	17.5
	45-65	33.6
	>65	48.7
	Unknown	0.3
Body mass index in kg/m²	<20	3.8
	20-25	13.0
	25-35	27.8
	>35	7.4
	Unknow	47.9
Sex at birth	Female	44.8
	Male	55.2
Severity	Dead	4.4
	Severe	21.8
	Moderate	51.0
	Mild	11.8
	Unknown	10.9
Oxygen therapy	Yes	48.2
	No	21.0
	Unknown	30.8
Ventilatory support	Yes	47.6
	No	14.0
	Unknown	38.5
Admission to intensive care unit	Yes	17.5
	No	33.6
	Unknown	48.7

617

618 **Table 2:** Reactome pathways associated with EP6, based on expression of aptamers. KnowEnG
619 analytical platform was used. The p-values were calculated using a one-sided Fisher's exact test
620 and were corrected for multiple tests using Benjamini-Hochberg method. Only signaling
621 pathways with FDR<5E-4 are shown in this table (see Table S4 for the full list).
622

Pathway	FDR
Signaling by Interleukins	2.75E-12
Cytokine Signaling in Immune system	6.25E-10
Immune System	2.28E-06
Signaling by FGFR	4.75E-06
Constitutive Signaling by Aberrant PI3K in Cancer	2.94E-05
FGFR2 ligand binding and activation	5.77E-05
Extracellular matrix organization	1.85E-04
FGFR3 ligand binding and activation	1.85E-04
FGFR3c ligand binding and activation	1.85E-04
FGFRL1 modulation of FGFR1 signaling	1.85E-04
TNFs bind their physiological receptors	2.58E-04
PI3K/AKT Signaling in Cancer	3.28E-04
PI5P, PP2A and IER3 Regulate PI3K/AKT Signaling	4.14E-04
Interleukin-4 and 13 signaling	4.91E-04

623
624

625 **Table 3**: SNVs differentiating EP6 against all other endophenotype clusters.

SNV ID	Position	Gene Symbol	SNV [1]	MAF	HWE	OR [2]	p-value
rs1394671	chr5:7348567	-	G > A	0.240	0.095	2.28	2.41E-06
rs12186698	chr5:168880668	*SLIT3*	T > C	0.087	0.247	2.93	3.72E-06
rs11625406	chr14:50049474	-	C > A	0.438	0.137	0.47	1.03E-05
rs11862889	chr16:83828886	-	T > C	0.104	0.446	2.62	1.07E-05
rs2995918	chr4:37905775	*TBC1D1*	C > T	0.494	0.776	0.49	1.20E-05
rs16897810	chr5:68415296	-	G > A	0.093	0.001	2.67	1.43E-05
rs2376263	chr17:35436659	*SLFN13*	G > A	0.261	0.073	2.01	2.48E-05
rs4790712	chr17:1614620	*SLC43A2*	G > A	0.441	0.003	1.97	2.50E-05
rs2294566	chr20:41472939	*CHD6*	C > A	0.239	0.265	2.04	2.78E-05
rs7164451	chr15:48921859	*SHC4*	G > A	0.386	0.053	1.89	3.01E-05
rs57664621	chr8:22808443	*PEBP4*	G > C	0.174	0.016	2.16	3.07E-05
rs28482919	chr3:14903094	*FGD5*	T > C	0.187	0.053	0.32	3.20E-05
rs6559283	chr9:89712560	-	T > C	0.375	<0.001	1.96	3.27E-05
rs657075	chr5:132094425	-	A > G	0.104	0.328	2.49	4.28E-05
rs56235109	chr15:62424001	*TLN2*	A > G	0.235	0.366	0.38	4.67E-05
rs7620057	chr3:179473377	*GNB4*	T > C	0.099	1.000	2.51	4.67E-05
rs10466868	chr12:131455375	-	T > G	0.108	0.401	2.51	5.94E-05
rs2236798	chr1:18735127	*PAX7*	A > G	0.054	0.114	2.90	6.11E-05
rs3774814	chr4:5464702	*STK32B*	C > G	0.205	<0.001	0.36	6.75E-05
rs4497815	chr19:22903215	-	G > A	0.216	0.205	2.07	7.52E-05
rs6765694	chr3:54601810	*CACNA2D3*	G > A	0.404	0.833	0.51	7.66E-05
rs2797773	chr6:37559045	-	C > T	0.422	0.000	0.53	8.06E-05
rs17014760	chr4:129419725	-	A > A	0.316	0.000	1.89	9.33E-05
rs10948260	chr6:45835559	-	G > A	0.366	0.189	1.81	9.52E-05
rs12035677	chr1:232391209	-	A > G	0.063	0.000	3.02	9.95E-05

626 Abbreviations used: SNV = Single nucleotide variation, HWE = Hardy Weinberg Equilibrium, MAF
627 = Minor allele frequency, OR = Odd ratio.
628
629 [1] SNV are described following GWAS annotations: refence allele > alternative allele (e.g., G > A).
630 [2] Logistic regression analyses using additive model adjusted for the 2 principal components.
631

632 **Table 4:** Association between genotypes and aptamer expression levels

SNV	Gene Symbol	Nearest gene	Aptamers normalized expression [1]				Multiple logistic regression analyses [3]			
			HM_{ref}	**HTZ**	**HM_{alt}**	p-val [2]	**Aptamers** OR	p-val	**SNV** OR	p-val
rs6765694	*CACNA2D3*	-	-0.09 (±0.89)	0.01 (±1.10)	0.24 * (±0.99)	**0.011**	0.61 (0.46-0.79)	2.5E-4	0.52 (0.37-0.74)	2.4E-4
rs10948260	-	*CLIC5*	0.02 (±0.92)	0.02 (±1.09)	-0.02 (±0.97)	0.796	0.68 (0.55-0.83)	1.7E-4	1.83 (1.35-2.48)	8.8E-5
rs657075	-	*IL3*	-0.01 (±1.01)	0.05 (±0.99)	0.32 (±0.46)	0.328	1.37 (1.14-11.64)	8.2E-4	2.49 (1.60-3.88)	5.2E-5
rs7164451	*SHC4*	-	-0.07 (±0.90)	0.01 (±1.05)	0.23 * (±1.16)	**0.017**	11.98 (7.61-18.87)	8.4E-27	2.00 (1.30-3.09)	1.8E-3
rs12186698	*SLIT3*	-	0.00 (±1.02)	0.07 (±1.06)	0.15 (±0.89)	0.509	0.82 (0.64-1.06)	0.135	2.99 (1.89-4.73)	2.7E-6
rs56235109	*TLN2*	-	-0.03 (±0.98)	0.06 (±1.03)	0.04 (±1.27)	0.353	0.58 (0.45-0.75)	2.7E-5	0.38 (0.23-0.60)	4.7E-5

633 Abbreviations used: SNV = Single nucleotide variation, HM_{ref} = Homozygotes for the reference
634 allele, HM_{alt} = Homozygotes for the alternative allele, HTZ = Heterozygotes, OR = Odd ratio.
635
636 [1] Aptamers' normalized levels of expression are reported as mean (± standard deviation).
637 Normalization steps for aptamer expressions are described in Methods.
638 [2] p-value, standard ANOVA analyses followed by Tukey *post hoc* analyses. Asterisks (*) identify
639 difference between HM_{ref} and HM_{alt} genotypes.
640 [3] Multiple logistic regression analyses models include aptamers expression values, SNV
641 genotypes (additive model) and the two principal components. OR are reported with 95%
642 confidence intervals in parentheses.
643
644

Table 5: Summary of the characteristics of each endophenotype.
In this table, High (Low), denoted as H (L) implies that the average value of the variable in the corresponding EP was significantly higher (lower) than the other EPs (considered together), while N (Nondescript) implies that it was not significantly different. The table is formed based on results described in Tables S1, S3 and S5.

Endophenotype	Age	Sex at birth	BMI	Metabolic sub-pathways	Blood markers
EP1	H	F	N	Leucine, Isoleucine and Valine Metabolism	High lymphocyte, Low neutrophil
EP2	N	N	L	N	High albumin, Low white blood cells
EP3	L	M	N	Phospholipid Metabolism	High platelet, Low creatinine
EP4	N	N	N	Ascorbate and Aldarate Metabolism	High lactate deshydrogenase
EP5	H	N	N	Benzoate Metabolism	High creatinine, Low haemoglobin
EP6	N	M	N	Methionine, Cysteine, SAM and Taurine Metabolism	High white blood cells, Low lymphocyte

Abbreviations used: H = High, L = Low, N = Nondescript, F = Female, M = Male

652 **References**

653 Agarwal, B., Gatt, A., Riddell, A., Wright, G., Chowdary, P., Jalan, R., Burroughs, A.K., and
654 Davenport, A. (2013). Hemostasis in patients with acute kidney injury secondary to acute liver
655 failure. Kidney International *84*, 158-163. https://doi.org/10.1038/ki.2013.92.

656 Al-Hadrawi, D.S., Al-Rubaye, H.T., Almulla, A.F., Al-Hakeim, H.K., and Maes, M. (2022). Lowered
657 oxygen saturation and increased body temperature in acute COVID-19 largely predict chronic
658 fatigue syndrome and affective symptoms due to Long COVID: A precision nomothetic approach.
659 Acta Neuropsychiatr, 1-12. 10.1017/neu.2022.21.

660 Ataga, K.I. (2009). Hypercoagulability and thrombotic complications in hemolytic anemias.
661 Haematologica *94*, 1481-1484. 10.3324/haematol.2009.013672.

662 Barnes, B.J., Adrover, J.M., Baxter-Stoltzfus, A., Borczuk, A., Cools-Lartigue, J., Crawford, J.M.,
663 Daßler-Plenker, J., Guerci, P., Huynh, C., and Knight, J.S. (2020). Targeting potential drivers of
664 COVID-19: Neutrophil extracellular traps. Journal of Experimental Medicine *217*.

665 Berrettini, W.H. (2005). Genetic bases for endophenotypes in psychiatric disorders. Dialogues
666 Clin Neurosci *7*, 95-101. 10.31887/DCNS.2005.7.2/wberrettini.

667 Blachier, F., Andriamihaja, M., and Blais, A. (2020). Sulfur-Containing Amino Acids and Lipid
668 Metabolism. The Journal of Nutrition *150*, 2524S-2531S. 10.1093/jn/nxaa243.

669 Blasco, A., Coronado, M.-J., Hernández-Terciado, F., Martín, P., Royuela, A., Ramil, E., García, D.,
670 Goicolea, J., Del Trigo, M., and Ortega, J. (2021). Assessment of neutrophil extracellular traps in
671 coronary thrombus of a case series of patients with COVID-19 and myocardial infarction. JAMA
672 cardiology *6*, 469-474.

673 Blatti III, C., Emad, A., Berry, M.J., Gatzke, L., Epstein, M., Lanier, D., Rizal, P., Ge, J., Liao, X., and
674 Sobh, O. (2020). Knowledge-guided analysis of "omics" data using the KnowEnG cloud platform.
675 PLoS biology *18*, e3000583. 10.1371/journal.pbio.3000583.

676 Bonaventura, A., Vecchié, A., Dagna, L., Martinod, K., Dixon, D.L., Van Tassell, B.W., Dentali, F.,
677 Montecucco, F., Massberg, S., and Levi, M. (2021). Endothelial dysfunction and
678 immunothrombosis as key pathogenic mechanisms in COVID-19. Nature Reviews Immunology
679 *21*, 319-329.

680 Bussolari, C., Palumbo, D., Fominsky, E., Nardelli, P., De Lorenzo, R., Vitali, G., De Cobelli, F.,
681 Rovere-Querini, P., and Scandroglio, A.M. (2021). Case Report: Nintedaninb May Accelerate Lung
682 Recovery in Critical Coronavirus Disease 2019. Frontiers in Medicine *8*, 766486.

683 Desilles, J.P., Solo Nomenjanahary, M., Consoli, A., Ollivier, V., Faille, D., Bourrienne, M.C.,
684 Hamdani, M., Dupont, S., Di Meglio, L., and Escalard, S. (2022). Impact of COVID-19 on thrombus
685 composition and response to thrombolysis: Insights from a monocentric cohort population of

686 COVID-19 patients with acute ischemic stroke. Journal of Thrombosis and Haemostasis *20*, 919-
687 928.

688 Ding, J., Hostallero, D.E., El Khili, M.R., Fonseca, G.J., Milette, S., Noorah, N., Guay-Belzile, M.,
689 Spicer, J., Daneshtalab, N., and Sirois, M. (2021). A network-informed analysis of SARS-CoV-2 and
690 hemophagocytic lymphohistiocytosis genes' interactions points to Neutrophil extracellular traps
691 as mediators of thrombosis in COVID-19. PLoS Computational Biology *17*, e1008810.
692 10.1371/journal.pcbi.1008810.

693 Durinck, S., Spellman, P.T., Birney, E., and Huber, W. (2009). Mapping identifiers for the
694 integration of genomic datasets with the R/Bioconductor package biomaRt. Nature Protocols *4*,
695 1184-1191. 10.1038/nprot.2009.97.

696 Emad, A., Ray, T., Jensen, T.W., Parat, M., Natrajan, R., Sinha, S., and Ray, P.S. (2020). Superior
697 breast cancer metastasis risk stratification using an epithelial-mesenchymal-amoeboid transition
698 gene signature. Breast Cancer Research *22*, 74. 10.1186/s13058-020-01304-8.

699 Englert, H., Rangaswamy, C., Deppermann, C., Sperhake, J.-P., Krisp, C., Schreier, D., Gordon, E.,
700 Konrath, S., Haddad, M., and Pula, G. (2021). Defective NET clearance contributes to sustained
701 FXII activation in COVID-19-associated pulmonary thrombo-inflammation. EBioMedicine *67*,
702 103382.

703 Esaki, Y., Hirokawa, K., Fukazawa, T., and Matsuda, T. (1984). Immunohistochemical study on the
704 liver in autopsy cases with disseminated intravascular coagulation (DIC) with reference to
705 clinicopathological analysis. Virchows Archiv A *404*, 229-241.

706 Ford, L., Kennedy, A.D., Goodman, K.D., Pappan, K.L., Evans, A.M., Miller, L.A.D., Wulff, J.E.,
707 Wiggs, B.R., III,, Lennon, J.J., Elsea, S., and Toal, D.R. (2020). Precision of a Clinical Metabolomics
708 Profiling Platform for Use in the Identification of Inborn Errors of Metabolism. The Journal of
709 Applied Laboratory Medicine *5*, 342-356. 10.1093/jalm/jfz026.

710 Gillespie, M., Jassal, B., Stephan, R., Milacic, M., Rothfels, K., Senff-Ribeiro, A., Griss, J., Sevilla, C.,
711 Matthews, L., Gong, C., et al. (2021). The reactome pathway knowledgebase 2022. Nucleic Acids
712 Research *50*, D687-D692. 10.1093/nar/gkab1028.

713 Gold, L., Ayers, D., Bertino, J., Bock, C., Bock, A., Brody, E., Carter, J., Cunningham, V., Dalby, A.,
714 and Eaton, B. (2010). Aptamer-based multiplexed proteomic technology for biomarker discovery.
715 Nature Precedings, 1-1.

716 Han, G., Gupta, S.D., Gable, K., Niranjanakumari, S., Moitra, P., Eichler, F., Brown Jr, R.H., Harmon,
717 J.M., and Dunn, T.M. (2009). Identification of small subunits of mammalian serine
718 palmitoyltransferase that confer distinct acyl-CoA substrate specificities. Proceedings of the
719 National Academy of Sciences *106*, 8186-8191.

720 Hull, D.L. (1974). Informal aspects of theory reduction. (Cambridge University Press), pp. 653-
721 670.

722 Kajita, K., Ishizuka, T., Miura, A., Kanoh, Y., Ishizawa, M., Kimura, M., Muto, N., and Yasuda, K.
723 (2001). Glucocorticoid-induced insulin resistance associates with activation of protein kinase C
724 isoforms. Cellular signalling *13*, 169-175.

725 Kaplan, E.L., and Meier, P. (1958). Nonparametric Estimation from Incomplete Observations.
726 Journal of the American Statistical Association *53*, 457-481. 10.1080/01621459.1958.10501452.

727 Kim, K., Chang, Y.-K., Bian, Y., Bae, O.-N., Lim, K.-M., and Chung, J.-H. (2018). Pro-coagulant and
728 pro-thrombotic effects of paclitaxel mediated by red blood cells. Thrombosis and Haemostasis
729 *118*, 1765-1775.

730 Lachkar, F., Ferré, P., Foufelle, F., and Papaioannou, A. (2021). Dihydroceramides: their emerging
731 physiological roles and functions in cancer and metabolic diseases. American Journal of
732 Physiology-Endocrinology and Metabolism *320*, E122-E130.

733 Leppkes, M., Knopf, J., Naschberger, E., Lindemann, A., Singh, J., Herrmann, I., Stürzl, M., Staats,
734 L., Mahajan, A., and Schauer, C. (2020). Vascular occlusion by neutrophil extracellular traps in
735 COVID-19. EBioMedicine *58*, 102925.

736 Liu, W., Peng, Y., and Tobin, D.J. (2013). A new 12-gene diagnostic biomarker signature of
737 melanoma revealed by integrated microarray analysis. PeerJ *1*, e49. 10.7717/peerj.49.

738 Lone, M.A., Hülsmeier, A.J., Saied, E.M., Karsai, G., Arenz, C., von Eckardstein, A., and Hornemann,
739 T. (2020). Subunit composition of the mammalian serine-palmitoyltransferase defines the
740 spectrum of straight and methyl-branched long-chain bases. Proceedings of the National
741 Academy of Sciences *117*, 15591-15598.

742 Luo, S., Feofanova, E.V., Tin, A., Tung, S., Rhee, E.P., Coresh, J., Arking, D.E., Surapaneni, A.,
743 Schlosser, P., Li, Y., et al. (2021). Genome-wide association study of serum metabolites in the
744 African American Study of Kidney Disease and Hypertension. Kidney International *100*, 430-439.
745 https://doi.org/10.1016/j.kint.2021.03.026.

746 MacDonald, J., and Sprecher, H. (1989). Distribution of arachidonic acid in choline-and
747 ethanolamine-containing phosphoglycerides in subfractionated human neutrophils. Journal of
748 Biological Chemistry *264*, 17718-17726.

749 Majumder, R., Liang, X., Quinn-Allen, M.A., Kane, W.H., and Lentz, B.R. (2011). Modulation of
750 prothrombinase assembly and activity by phosphatidylethanolamine. Journal of Biological
751 Chemistry *286*, 35535-35542.

752 Marees, A.T., de Kluiver, H., Stringer, S., Vorspan, F., Curis, E., Marie-Claire, C., and Derks, E.M.
753 (2018). A tutorial on conducting genome-wide association studies: Quality control and statistical
754 analysis. Int J Methods Psychiatr Res *27*, e1608. 10.1002/mpr.1608.

755 Marfia, G., Navone, S., Guarnaccia, L., Campanella, R., Mondoni, M., Locatelli, M., Barassi, A.,
756 Fontana, L., Palumbo, F., and Garzia, E. (2021). Decreased serum level of sphingosine-1-

757 phosphate: a novel predictor of clinical severity in COVID-19. EMBO molecular medicine *13*,
758 e13424.

759 Marshall, J.C., Murthy, S., Diaz, J., Adhikari, N., Angus, D.C., Arabi, Y.M., Baillie, K., Bauer, M.,
760 Berry, S., and Blackwood, B. (2020). A minimal common outcome measure set for COVID-19
761 clinical research. The Lancet Infectious Diseases *20*, e192-e197.

762 Middleton, E.A., He, X.-Y., Denorme, F., Campbell, R.A., Ng, D., Salvatore, S.P., Mostyka, M.,
763 Baxter-Stoltzfus, A., Borczuk, A.C., and Loda, M. (2020). Neutrophil extracellular traps contribute
764 to immunothrombosis in COVID-19 acute respiratory distress syndrome. Blood *136*, 1169-1179.

765 Murtagh, F., and Legendre, P. (2014). Ward's Hierarchical Agglomerative Clustering Method:
766 Which Algorithms Implement Ward's Criterion? Journal of Classification *31*, 274-295.
767 10.1007/s00357-014-9161-z.

768 Obermayer, A., Jakob, L.-M., Haslbauer, J.D., Matter, M.S., Tzankov, A., and Stoiber, W. (2021).
769 Neutrophil extracellular traps in fatal COVID-19-associated lung injury. Disease markers *2021*.

770 Ochoa, A. (2022). genio: Genetics Input/Output Functions. R package version 1.1.1.
771 https://CRAN.R-project.org/package=genio.

772 Ouwendijk, W.J., Raadsen, M.P., Van Kampen, J.J., Verdijk, R.M., Von Der Thusen, J.H., Guo, L.,
773 Hoek, R.A., Van Den Akker, J.P., Endeman, H., and Langerak, T. (2021). High levels of neutrophil
774 extracellular traps persist in the lower respiratory tract of critically ill patients with coronavirus
775 disease 2019. The Journal of infectious diseases *223*, 1512-1521.

776 Papageorgiou, C., Jourdi, G., Adjambri, E., Walborn, A., Patel, P., Fareed, J., Elalamy, I.,
777 Hoppensteadt, D., and Gerotziafas, G.T. (2018). Disseminated intravascular coagulation: an
778 update on pathogenesis, diagnosis, and therapeutic strategies. Clinical and Applied
779 Thrombosis/Hemostasis *24*, 8S-28S.

780 Parman, T., Bunin, D.I., Ng, H.H., McDunn, J.E., Wulff, J.E., Wang, A., Swezey, R., Rasay, L.,
781 Fairchild, D.G., and Kapetanovic, I.M. (2011). Toxicogenomics and metabolomics of
782 pentamethylchromanol (PMCol)-induced hepatotoxicity. Toxicological Sciences *124*, 487-501.

783 Perdry, H., and Dandine-Roulland, C. (2020). gaston: Genetic Data Handling (QC, GRM, LD, PCA)
784 & Linear Mixed Models. R package version 1.5.7. https://CRAN.R-project.org/package=gaston.

785 Petito, E., Falcinelli, E., Paliani, U., Cesari, E., Vaudo, G., Sebastiano, M., Cerotto, V., Guglielmini,
786 G., Gori, F., and Malvestiti, M. (2021). Association of neutrophil activation, more than platelet
787 activation, with thrombotic complications in coronavirus disease 2019. The Journal of infectious
788 diseases *223*, 933-944.

789 Pirnes-Karhu, S., Jantunen, E., Mäntymaa, P., Mustjoki, S., Alhonen, L., and Uimari, A. (2014).
790 Spermidine/spermine N1-acetyltransferase activity associates with white blood cell count in
791 myeloid leukemias. Experimental Hematology *42*, 574-580.

792 Port, J.R., Adney, D.R., Schwarz, B., Schulz, J.E., Sturdevant, D.E., Smith, B.J., Avanzato, V.A.,
793 Holbrook, M.G., Purushotham, J.N., and Stromberg, K.A. (2021). High-fat high-sugar diet-induced
794 changes in the lipid metabolism are associated with mildly increased COVID-19 severity and
795 delayed recovery in the Syrian hamster. Viruses *13*, 2506.

796 R Core Team (2022). R: A Language and Environment for Statistical Computing. (R Foundation for
797 Statistical Computing). https://www.R-project.org/.

798 Ran, S., Downes, A., and Thorpe, P.E. (2002). Increased exposure of anionic phospholipids on the
799 surface of tumor blood vessels. Cancer research *62*, 6132-6140.

800 Rubin, R. (2020). As their numbers grow, COVID-19 “long haulers” stump experts. Jama *324*,
801 1381-1383.

802 Russell, C.D., and Baillie, J.K. (2017). Treatable traits and therapeutic targets: goals for systems
803 biology in infectious disease. Current opinion in systems biology *2*, 140-146.

804 Sato, K., Iemitsu, M., Aizawa, K., and Ajisaka, R. (2008). Testosterone and DHEA activate the
805 glucose metabolism-related signaling pathway in skeletal muscle. American Journal of
806 Physiology-Endocrinology and Metabolism *294*, E961-E968.

807 Satopaa, V., Albrecht, J., Irwin, D., and Raghavan, B. (2011). Finding a" kneedle" in a haystack:
808 Detecting knee points in system behavior. (IEEE), pp. 166-171.

809 Sinauridze, E.I., Kireev, D.A., Popenko, N.Y., Pichugin, A.V., Panteleev, M.A., Krymskaya, O.V., and
810 Ataullakhanov, F.I. (2007). Platelet microparticle membranes have 50-to 100-fold higher specific
811 procoagulant activity than activated platelets. Thrombosis and haemostasis *97*, 425-434.

812 Skendros, P., Mitsios, A., Chrysanthopoulou, A., Mastellos, D.C., Metallidis, S., Rafailidis, P.,
813 Ntinopoulou, M., Sertaridou, E., Tsironidou, V., and Tsigalou, C. (2020). Complement and tissue
814 factor–enriched neutrophil extracellular traps are key drivers in COVID-19 immunothrombosis.
815 The Journal of clinical investigation *130*, 6151-6157.

816 Smadja, D.M., Philippe, A., Bory, O., Gendron, N., Beauvais, A., Gruest, M., Peron, N., Khider, L.,
817 Guerin, C.L., and Goudot, G. (2021). Placental growth factor level in plasma predicts COVID-19
818 severity and in-hospital mortality. Journal of Thrombosis and Haemostasis *19*, 1823-1830.

819 Stafford, J.H., and Thorpe, P.E. (2011). Increased exposure of phosphatidylethanolamine on the
820 surface of tumor vascular endothelium. Neoplasia *13*, 299-IN292.

821 Tavoosi, N., Davis-Harrison, R.L., Pogorelov, T.V., Ohkubo, Y.Z., Arcario, M.J., Clay, M.C., Rienstra,
822 C.M., Tajkhorshid, E., and Morrissey, J.H. (2011). Molecular Determinants of Phospholipid
823 Synergy in Blood Clotting *. Journal of Biological Chemistry *286*, 23247-23253.
824 10.1074/jbc.M111.251769.

825 Te Pas, M.F.W., Madsen, O., Calus, M.P.L., and Smits, M.A. (2017). The Importance of
826 Endophenotypes to Evaluate the Relationship between Genotype and External Phenotype.
827 International Journal of Molecular Sciences *18*, 472.

828 Thomas, T., Stefanoni, D., Reisz, J.A., Nemkov, T., Bertolone, L., Francis, R.O., Hudson, K.E.,
829 Zimring, J.C., Hansen, K.C., and Hod, E.A. (2020). COVID-19 infection alters kynurenine and fatty
830 acid metabolism, correlating with IL-6 levels and renal status. JCI insight *5*.

831 Tremblay, K., Rousseau, S., Zawati, M.n.H., Auld, D., Chassé, M., Coderre, D., Falcone, E.L.,
832 Gauthier, N., Grandvaux, N., and Gros-Louis, F. (2021). The Biobanque québécoise de la COVID-
833 19 (BQC19)—A cohort to prospectively study the clinical and biological determinants of COVID-
834 19 clinical trajectories. PloS one *16*, e0245031. 10.1371/journal.pone.0245031.

835 Ward Jr, J.H. (1963). Hierarchical grouping to optimize an objective function. Journal of the
836 American statistical association *58*, 236-244.

837 Warnes, G., Gorjanc, G., Leisch, F., and Man, M. (2021). genetics: Population Genetics. R package
838 version 1.3.8.1.3. https://CRAN.R-project.org/package=genetics.

839 Williams, R., Schalm, S.W., and O'Grady, J.G. (1993). Acute liver failure: redefining the syndromes.
840 The Lancet *342*, 273-275. https://doi.org/10.1016/0140-6736(93)91818-7.

841 Ye, C., Sutter, B.M., Wang, Y., Kuang, Z., and Tu, B.P. (2017). A metabolic function for phospholipid
842 and histone methylation. Molecular cell *66*, 180-193. e188.

843 Zahedi, K., Barone, S., Kramer, D.L., Amlal, H., Alhonen, L., Jänne, J., Porter, C.W., and Soleimani,
844 M. (2010). The role of spermidine/spermine N 1-acetyltransferase in endotoxin-induced acute
845 kidney injury. American Journal of Physiology-Cell Physiology *299*, C164-C174.

846 Zheng, X., Levine, D., Shen, J., Gogarten, S.M., Laurie, C., and Weir, B.S. (2012). A high-
847 performance computing toolset for relatedness and principal component analysis of SNP data.
848 Bioinformatics *28*, 3326-3328. 10.1093/bioinformatics/bts606.

849 Zhou, S., Butler-Laporte, G., Nakanishi, T., Morrison, D.R., Afilalo, J., Afilalo, M., Laurent, L.,
850 Pietzner, M., Kerrison, N., Zhao, K., et al. (2021). A Neanderthal OAS1 isoform protects individuals
851 of European ancestry against COVID-19 susceptibility and severity. Nature Medicine *27*, 659-667.
852 10.1038/s41591-021-01281-1.

853